Investigating the Spin Dynamics of Spin-Triplet Cooper Pairs

Ruigrok, Jesse

.

Investigating the Spin Dynamics of Spin-Triplet Cooper Pairs

THESIS

submitted in partial fulfillment of the
requirements for the degree of

BACHELOR OF SCIENCE
in
PHYSICS

Author :	Jesse Ruigrok
Student ID :	1816055
Supervisor :	Tycho Blom
	Kaveh Lahabi
Second corrector :	Jan Aarts

Leiden, The Netherlands, July 15, 2024

Investigating the Spin Dynamics of Spin-Triplet Cooper Pairs

Jesse Ruigrok

Huygens-Kamerlingh Onnes Laboratory, Leiden University
P.O. Box 9500, 2300 RA Leiden, The Netherlands

July 15, 2024

Abstract

On the hunt for spin triplet superconductivity in ferromagnet-superconductor multilayers, additions were made to an RF insert with an open co-planar waveguide. The low loss setup, with a -1dB per GHz characteristic, was used to obtain FMR spectra with a vector network analyzer. A superconducting coil was designed to generate magnetic fields in situ at cryogenic temperatures. Many cobalt-niobium thin film multilayers were created by means of e-beam evaporation. The FMR spectra were recorded at room temperature and cryogenic temperatures as low as 4.5K. The spectra were analyzed to determine the linewidth of the FMR resonance above and below the critical temperature of different thicknesses of the superconducting layer. The initial results are promising, but not sufficient to conclude decreased gilbert damping in the ferromagnet below the T_c of the superconductor.

Contents

Chapter 1

Introduction

Superconductivity continues to produce thought provoking discoveries. Electron transport without energy dissipation is a core property of superconducting materials and has led to many groundbreaking innovations. Electrons do not only carry charge across materials, but spin as well. Spin is an intrinsic property of particles that describes their internal angular momentum. Electrons belong to the class of spin $\frac{1}{2}$ fermions and within superconductors they come together to form cooper pairs. These cooper pairs require antisymmetric pairing and were long believed to exist only as opposite spin pairings, or 'singlet' states. This exclusion principle can be overcome by attaining antisymmetry through another component: the momentum or frequency of the electrons. Cooper pairs of equal spin can thereby be formed through these alternative pairings, creating spin triplets. A huge potential is unlocked by net-spin carrying triplet states. It is where the fields of superconductivity and spintronics meet. Like singlet states, non-polarized triplets are pulled apart by the exchange interaction inside ferromagnets. The triplet states however, can become spin polarized by a spin rotation process. The generation and control over spin polarized currents has a great many applications in modern technology, making spintronics an ever-relevant field. The long-standing research into spin currents almost celebrates a decade's existence. The field drew new breath when non-collinear ferromagnetic multilayers were found to generate long range triplet correlations. Work has been done to create such misaligned ferromagnetic structures. This led to interest in spin textured devices and recently Lahabi et al.(2018) [13] have shown dynamic control of triplet supercurrents by using a ferromagnetic vortex in a cobalt disk. Further research to these correlations has largely been done in Josephson junctions, for example by Bell et al.(2008) [2]

The goal of this project is to simplify research into long range triplet currents by way of a hands-on method to obtain FMR resonance spectra in thin films. By successfully showing the presence of triplet currents in FM-SC multilayers, we open many lines of inquiry into the inner workings of superconducting materials and can start to probe the more exotic composites. This thesis will lay a part of that groundwork. First, the basic concepts that are important for understanding the dynamics of magnetic systems are explained. Some common measurement methods and the unavoidable technical language will be introduced. This is finished with the explanation of a piece of research into spin triplets that is indicative of our line of inquiry. The third chapter describes and characterises the equipment used for obtaining FMR spectra. Additionally, the samples to be put under test are listed. Then, the initial results at room temperature are presented. The discussion of these results informs alterations to the measurement methodology. One of the additions is a superconducting coil designed specifically to produce local, homogenous magnetic fields. This design process will be explained in the fifth chapter. Then the stage is set to present the FMR spectra taken at cryogenic temperatures. The resulting linewidth measurements will be discussed and conclusions are drawn. Lastly, a critical look is taken at further steps to potential research.

Chapter 2

Theory

2.1 Ferromagnetic Dynamics

Magnetism at the macro scale is the result of smaller interacting magnetic moments inside the material. These neighbouring elements can interact through many pathways and lead to a great number of complex behaviours. Generally, a magnetic system will tend toward a minimum in the total of the free energy.

$$E_{total} = \int \epsilon_{ex} + \epsilon_{an} + \epsilon_{dem} + \epsilon_{Zee} + \epsilon_{stress} + \epsilon_{ms}\, dV \tag{2.1}$$

The first term is due to the exchange interaction between magnetic moments. Second is the anisotropic energy, which is determined by the crystal structure of the material. Third is the demagnetization energy, which increases with the strength of stray fields in an effort to locally align moments parallel to the edge of the material. Fourth is the Zeeman energy due to an applied external field and defines properties as the hysteresis loop of the material. Lastly, are the terms for mechanical stress applied to the material and magnetostriction [5].
Specifically in ferromagnets, the exchange interaction between electron spins drives them to order in parallel and gives rise to an overall magnetization. To simplify the inner workings of a magnetic system, we can consider only the combined magnetization vector, as depicted in Figure 2.1a

$$\frac{d\mathbf{M}}{dt} = -\gamma \mathbf{M} \times \mathbf{H} + \frac{\alpha}{M_s} \mathbf{M} \times \frac{d\mathbf{M}}{dt} \tag{2.2}$$

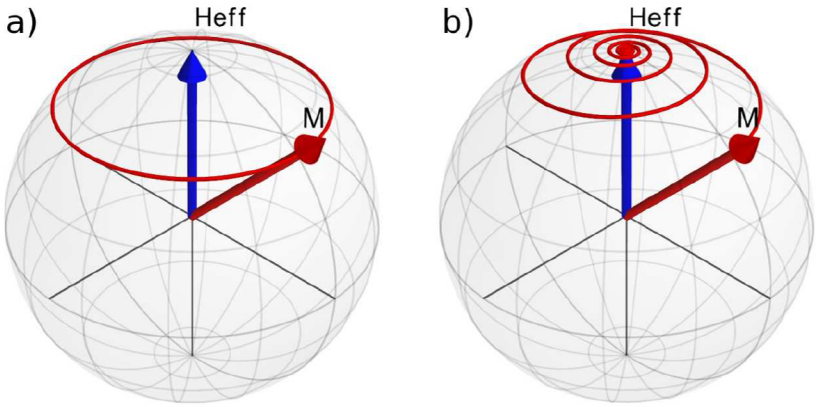

Figure 2.1: *Schematic showing the precession of the magnetization vector* **M** *around a local field* H_{eff}. ***a)*** *shows the precession when no net damping is present.* ***b)*** *shows how damping realigns* **M** *with the local field. Image from Verhagen(2014) [22]*

Here **M** is the magnetization of the magnetic system, **H** is the effective local magnetic field. Parameter γ is the gyromagnetic ratio, α is the Gilbert damping factor and M_s is the material dependent saturation magnetization. The first term in equation 2.2 describes how the magnetization will tend to rotate around any effective local field present inside the system and is known as the precession term. Additionally, the magnetization will tend to align with the local field as shown in schematic 2.1b. The strength of this damping term is determined by the prefactor $\frac{\alpha}{M_s}$. We can therefore describe the dynamic relaxation of the magnetic system by closely examining the damping factor α. The LLGE is a powerfully simplistic formula to describe the complex dynamics of magnetic systems.

2.2 Spin Pumping

If we imagine a ferromagnetic system in equilibrium with the local field, an excitation of the effective field can bring the magnetization vector of the ferromagnet out of alignment. For this to work, the driving field needs a strong orthogonal component to the local field. As mentioned in the previous chapter, the overall magnetization will gyroscopically move around and align with the effective local field vector. This precession occurs at the Larmor frequency, which can be derived from the precession term in the

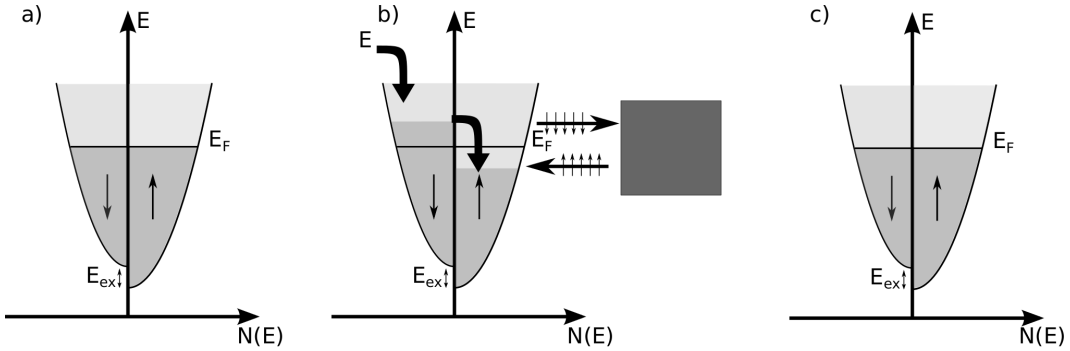

Figure 2.2: a) *shows the density of states of electron spin distribution. Both up and down states are filled up to the Fermi level E_F. In* ***b)*** *a ferromagnet imparts its momentum onto available electrons and introduces an imbalance in the distribution of spin states. Through spin flip relaxation the system can return to equilibrium. If an adjacent layer is present, the spin relaxation process can be accelerated by injecting a spin polarized current into this layer. From verhagen2014 [22], originally adapted from czeschka2011 [6]*

LLG equation:

$$\omega_{Larmor} = -\gamma H_{ext} \tag{2.3}$$

If, however, the local field is continuously excited at the Larmor frequency, we prevent the magnetization from relaxing over time and it will maintain gyroscopic motion. This is the working principle behind many magnetic resonance phenomena such as electron paramagnetic resonance (EPR), nuclear magnetic resonance (NMR) and ferromagnetic resonance (FMR).
The pathway through which the ferromagnet relaxes its magnetization is largely by spin-carrying electrons present in the material. The electrons exist within a distribution of up and down spin states. As the magnetization is imparted upon the electrons, a spin imbalance arises. In order to return to an equilibrium state, the electrons can undergo a process of spin flip relaxation, which is shown in more detail in Figure 2.2.
If the rate at which the ferromagnet induces a spin polarization onto the electrons exceeds the rate at which the spins can relax, a spin accumulation will build up in the ferromagnet. This spin polarized current can then move into an adjacent material in ohmic contact with the ferromagnet. This opens new pathways for the spins to relax, which in turn changes the dynamics which control the damping in the precession of the magnetization vector. This phenomenon is aptly named Spin Pumping.

2.3 Spectrum Analysis Methods

The characterization of an FMR resonance spectrum has been done through many different methods. Depending on measurement system and sample, a relatively broad range of frequencies is common for FMR spectra and is an important consideration for spectrum sampling. Other considerations are the number of active elements in the spectrometer, comparison of measurement and reference signals and the level of direct relation to the Gilbert damping factor. To extract a Gilbert damping factor from a broadband spectrum three techniques are most used, each exploiting a niche in these considerations. Each technique requires a method of applying a non-driving external field to control the resonance frequency of the FM and is usually fulfilled with Helmholtz coils.

PIMM
A method using a direct relaxation dynamic is the Pulsed Inductive Microwave Magnetometer (PIMM) technique. By modulating an input frequency source with a square wave on the order of Kilohertz a pulse generator is created that can 'flick' a FM sample with a short driving field. The relaxation of the FM over nanoseconds can then be measured using a high-frequency oscilloscope as shown in Figure 2.3. The absorption can be quantified through an FFT of the response after subtraction of a reference measurement. The reference signal is not easily obtained and involves saturating the FM in the same transverse orientation as the driving field to measure a reference without damping. An important application of this technique is found in Jeon et al [10], who circumvents the reference FFT by rectifying the signal using a diode to obtain a dc-voltage that can be compared to the input pulse. Thereby eliminating contributions of other frequencies from the measurement signal.

SL-FMR
Another method often encountered is field-variable FMR at a fixed driving frequency. This can be done with use of a microwave cavity or stripline. The cavity is supplied with a driving field matching the natural resonance frequency of the cavity. Although a cavity has a high quality factor, the resonance frequency and its sensitivity change upon introduction of an FM sample. The geometry of the cavity ensures uniformity of the driving field. The external field is varied to match the FM resonance to the tuned cavity. When the external field is varied around this resonance field an FMR spectrum can be measured from the return signal. Cavities are limited in their broadband frequency application. For low loss FM samples,

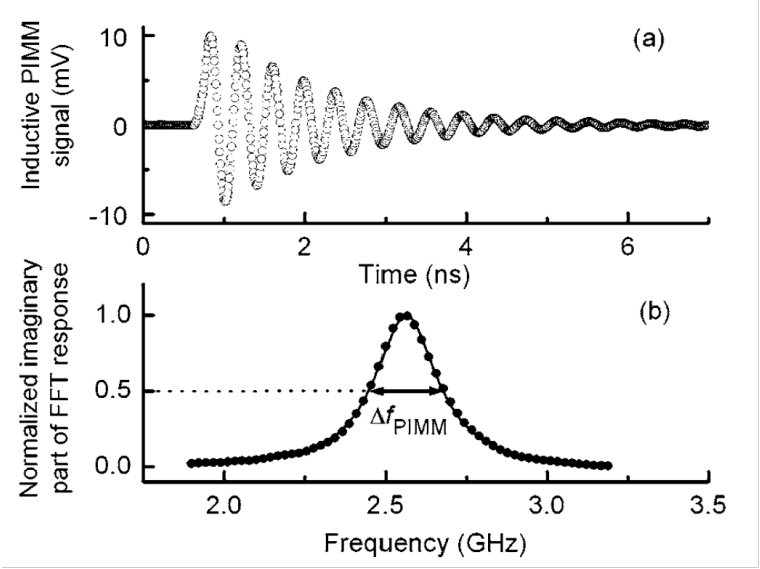

Figure 2.3: *Graph **(a)** shows a typical time response for an FM film sample in pulsed inductive microwave magnetometry (PIMM) measured by an high sample rate oscilloscope. Graph **(b)** shows the FFT of the response in **(a)** with a lorentzian fit and an indication of the full width half maximum (FWHM). Image from Kalarickal et al [12]*

the FMR resonance can couple to the cavity resonance and prohibit measurement [15]. Using a stripline in field-swept FMR eliminates the practical disadvantages of a cavity system, but both techniques suffer from the indirect relation to the Gilbert damping, which is defined by frequency broadening in the FMR spectrum. A measurement in field broadening of the spectrum requires conversion.

VNA-FMR

A method truly benefiting from its simplicity makes use of a vector network analyser (VNA) and a stripline such as a coplanar waveguide (CPW). A VNA can function both as a generator of a driving field and as a spectrum sampler. It does this by comparing output and return signals into S-parameters. In Figure 2.4 is shown how the signals at different ports are combined to 4 distinct measurement parameters. Specifically, the S_{21} parameter is a measure of the loss through the entirety of the connected system. To acquire a spectrum holding only contributions from an FM sample, a reference measurement must be made to subtract the microwave characteristics of the system. Furthermore, modern VNAs offer a wide range of operating frequencies, allowing higher frequency FMR spectra

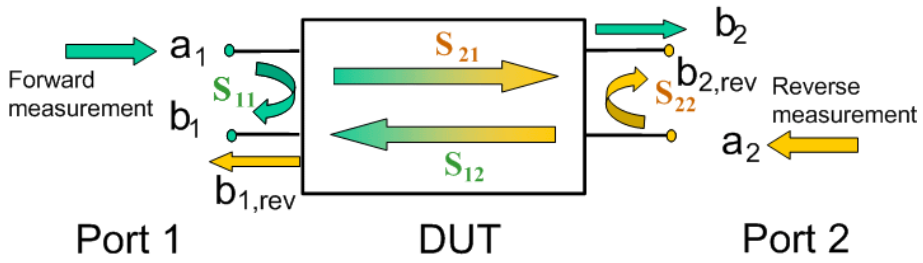

Figure 2.4: *Diagram showing the signal flow of a 2-port VNA in terms of S-parameters. Parameter S_{21} is defined as the forward transmission coefficient defined as the ratio between outgoing wave b_2 and incident wave a_1 under condition of no return transmission a_2. Image from Rhode&Schwarz [19].*

to be measured. It can be challenging to manage the impedance of the FM-coupled CPW as this can introduce frequency dependent distortion in the spectrum. Some distortions and offsets can be mitigated by considering phase shifts and reflection parameters, conveniently provided by the VNA. Analytically, spectra can be cleaned by fitting a Lorentzian distribution to a normalised absorption spectrum.
VNA-FMR has gained interest in recent years. Nano-fabricated magnetic systems and spintronics are important fields of study in modern technologies. As VNAs have had widespread use in systems diagnostics for microwave applications such as antennas and communication systems, commercially available VNAs are financially viable and offer a large number of capabilities. Since the turn of the century, more papers have been published on thin film FMR, a number of which make use of VNAs such as [17], [23], [7], [21]. For a more in-depth comparison between FMR methods the following sources are quite useful [12], [16].

2.4 Resonance Linewidths

With a direct relation between linewidth broadening and the gilbert damping, all that rests is defining the linewidth to be taken from absorption spectra. Many definitions exist, two of which will be highlighted and a third will be introduced.
The most common method, often used in bandwidth analysis, is the full width at half maximum (FWHM) definition. This definition is refreshingly self-explanatory, as it takes the width at half of the maximum absorption peak, similar to Figure 2.5. A second, very similar definition is the peak-to-peak width (ΔPP). This requires taking a derivative of the measured

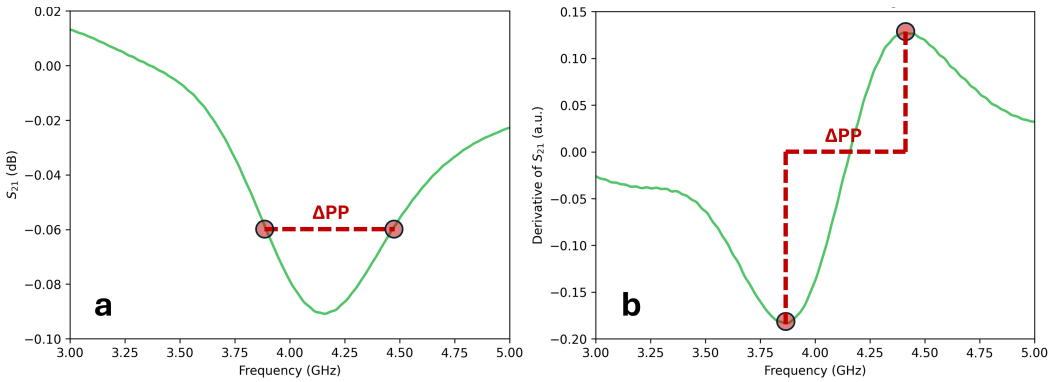

Figure 2.5: ***a*** *shows a typical FMR resonance spectrum.* ***b*** *shows the derivative of the spectrum in* ***a*** *and both have an indication of the ΔPP linewidth.*

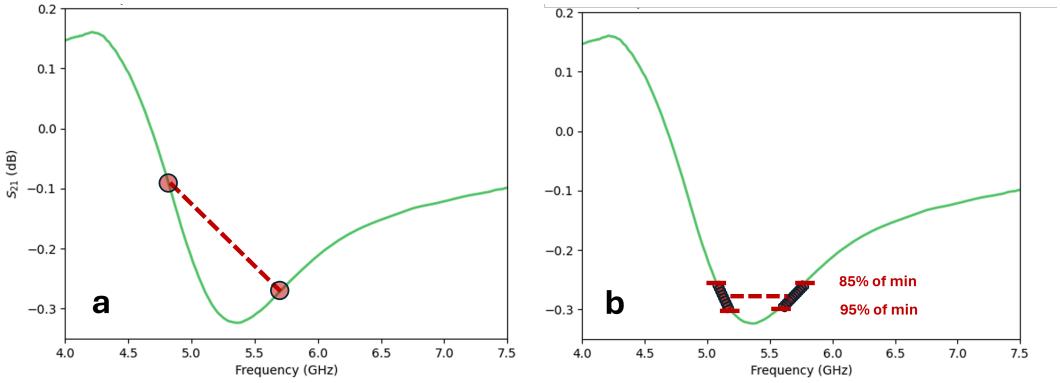

Figure 2.6: ***a*** *shows an asymmetrical FMR resonance spectrum with its equivalent indication of ΔPP linewidth.* ***b*** *shows the alternative 90-percent width definition of linewidth for the same spectrum as in* ***a****.*

spectrum and determining the distance between its maximum and minimum, thereby defining the linewidth in terms of the inflection points of the absorption spectrum.
Both methods are analytically easy to apply but require relatively clean spectra or necessitate fitting a distribution. Additionally, these methods are only well defined for symmetrical distributions. For asymmetrical spectra, the linewidth is skewed as shown in Figure 2.6a. To define a linewidth in such case with some measure of standardization, a 90-percent peak width will also be defined. The average between 85% and 95% of the maximum absorption peak is taken left and right of the resonance peak. The distance between these averages is than taken to be the 90-percent peak width. This process is shown in Figure 2.6b.
A method to compare frequency swept and field swept linewidths is out-

lined by Kalarickal2006. The FMR resonance peak positions are consistent across both type of measurements. By comparing the Kittel formulas in terms of $f_{Kittel}(H_{ext})$ and $H_{Kittel}(f)$ a conversion relation can be obtained.

$$\Delta H = \frac{\Delta f}{|\gamma| P_A(f)} \tag{2.4}$$

$$P_A(f) = \sqrt{1 + \left(\frac{|\gamma|\mu_0 M_s}{4\pi f}\right)^2} \tag{2.5}$$

Where ΔH is the field linewidth, Δf is the frequency linewidth and $P_A(f)$ is a conversion factor dependent on the resonance peak frequency.

2.5 F-N and F-S Heterostructures

To grasp the dynamics of spin polarised currents it is necessary to consider the interface between multiple different materials. These ferromagnetic multilayers, or heterostructures, are depicted in Figure 2.7.
The FM layer, upon excitation, generates a spin polarised current entering the adjacent material. In the case of an F-N multilayer, the normal metal gains an asymmetric spin distribution, that can equalize through many processes, primarily spin flip scattering. This then translates to an increased gilbert damping factor inside the FM layer, the strength of which is highly dependent on the material. The spin accumulation inside the normal metal occurs over a distance at which the normal metal effectively diffuses the spin current, the spin diffusion length λ_{sd}. In metals this length can range anywhere from a few nanometres to a few hundred nanometres. Naturally, this is the same process as occurs in a F-SC multilayer above the superconductor's critical temperature. Below the superconductors Tc, the electrons inside the SC layer form cooper pairs and the resulting superconducting energy gap prevents the spin polarised current from effectively penetrating the SC layer. However, due to the proximity effect at the interface with the FM layer, spins can accumulate over a distance of the superconducting coherence length ξ_{sc}. This can be understood as the length scale over which the wave characteristic will remain consistent while maintaining superconductivity. It is sometimes more plainly considered as the size of a coherent cooper pair. Generally, a large portion of the polarised spin current will be reflected at the F-SC interface, maintaining a damping factor close to the natural state of the FM layer. This means

that at the transition temperature a F-SC multilayer will experience a sudden drop in the gilbert damping or in other terms a decrease in spectrum linewidth.

Figure 2.8a shows the sudden drop in linewidth below Tc for different thicknesses of a niobium SC layer. This linewidth sharpening can be quite large. The difference between the above and below T_c linewidth increases with the thickness of the niobium, up to the diffusion length. There is also a characteristic increase in linewidth right before the transition. A peculiar effect happens when an additional layer is added beyond the SC layer, specifically of a material that is considered to be a good spin sink such as platinum. Platinum very effectively dissipates spin accumulation, boasting a spin diffusion length in the single digits. This is attributed to the large spin orbit coupling (SOC) platinum experiences. In these Pt capped multilayers, the linewidth broadens below T_c for Nb-layers thinner than the coherence length. This is shown by the plot in Figure 2.8b.
One explanation is the existence of long range spin triplet states across the FM and SC layers. Within the SC layer, there are singlet correlated cooper pairs that are a combination of equal and opposite spins ($|\uparrow\downarrow\rangle - |\downarrow\uparrow\rangle$). Additionally, there are triplet correlated cooper pairs once again with zero net spin projection ($|\uparrow\downarrow\rangle + |\downarrow\uparrow\rangle$). Both these cooper pair types exist partly within the FM layer. Neither are very long lived inside the FM layer, as the exchange interaction decouples the cooper pairs quickly. However, the triplet cooper pairs can be turned into a stable net-spin carrier through spin rotation ($|\uparrow\uparrow\rangle + |\downarrow\downarrow\rangle$). Experimentally, this has been done using multiple adjacent FM layers with non-collinear magnetization axes. Such FM 'spin mixing' layers create triplet states in one spin orientation as the perpendicularly magnetized FM layer rotates the triplet onto another plain. The multilayers in Figure 2.8 do not contain a spin mixing FM layer. It is predicted that the large SOC in combination with ferromagnetic exchange can also generate equal spin triplet correlations in multilayers [3]. These equal spin triplets are not pulled apart by the exchange interaction inside the FM and can carry a spin current. It is possible therefore that long range triplets can reach across the SC layer into the spin sink layer, where they are dissipated. As such, damping would increase and linewidth would broaden as presented. In theory, one could make many multilayers with different thicknesses of the SC-layer and by examining the FMR linewidth broadening, could deduce the coherence length of the SC material.

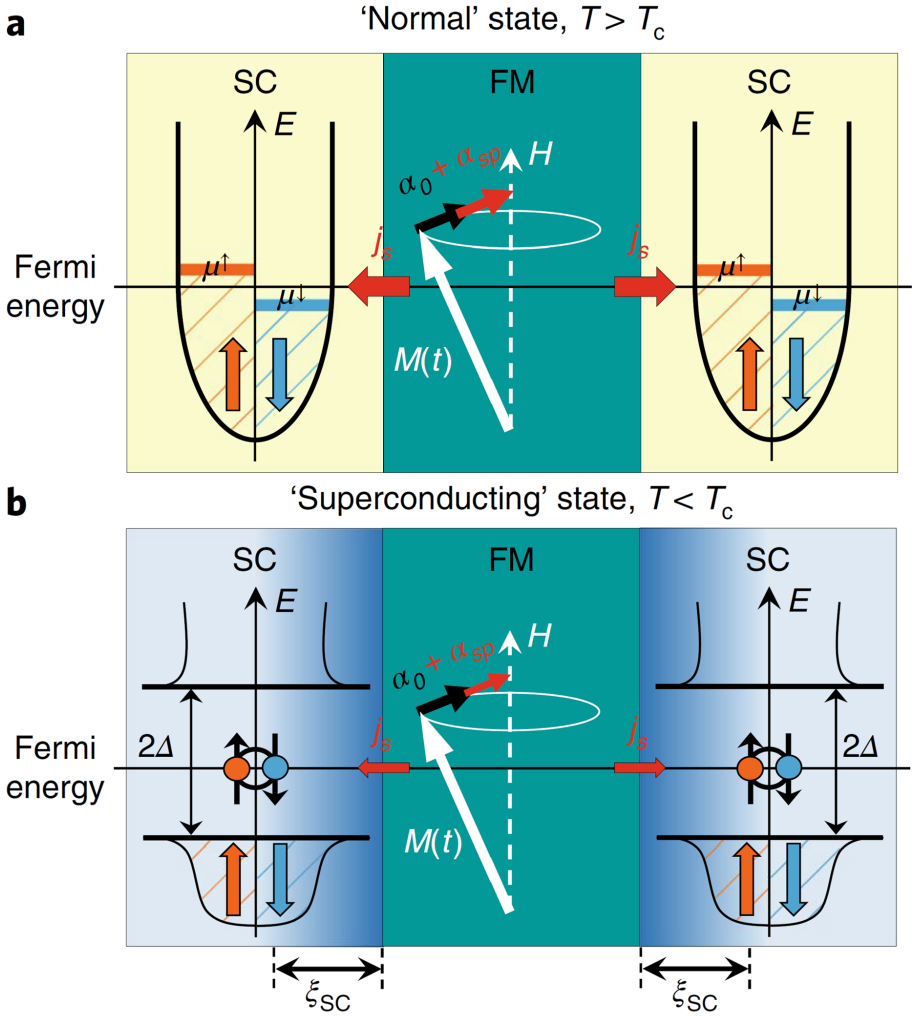

Figure 2.7: ***a*** *is a diagram showing the precessing magnetization vector* $\mathbf{M}(\mathbf{t})$ *generating a spin polarised current* J_s *into an adjacent normal metal, causing a local imbalance in spin distribution. This provides an additional gilbert damping contribution* α_{sp}*. below the transition temperature* T_c *in* ***b****, where the superconducting energy gap* 2Δ *prevents a spin polarized current from affecting the superconducter further than the coherence length* ξ_{sc}*. Borrowed from Jeon et al.(2018) [10].*

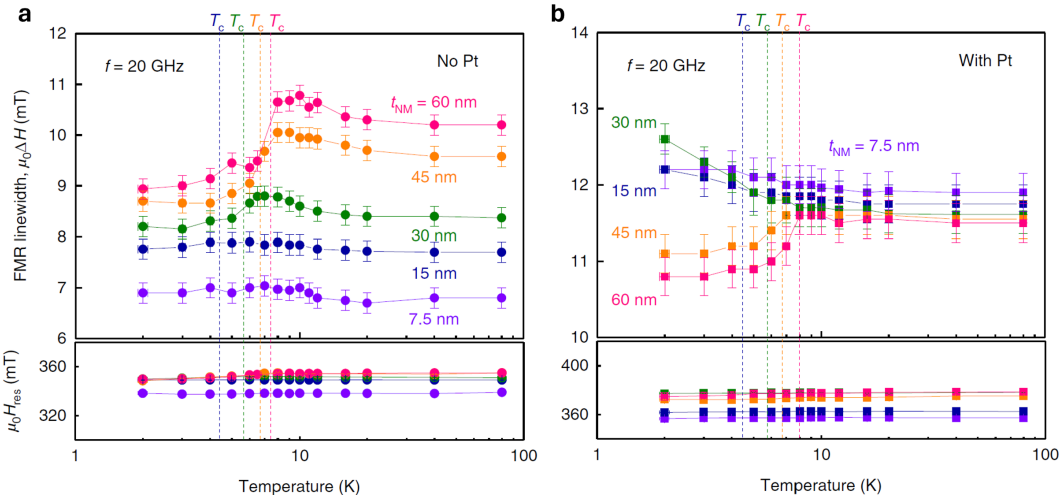

Figure 2.8: ***a*** *is the temperature dependence of the field swept FMR linewidth (FWHM) for Nb/Py/Nb samples for various Nb thicknesses obtained at 20GHz resonance. The dashed lines indicate T_c. On the bottom the resonance field for each datapoint is shown.* ***b*** *shows the equivalent of* ***a*** *for Pt/Nb/Py/Nb/Pt spin sink samples. Borrowed from Jeon et al.(2018) [10].*

Chapter 3

Setup

In this chapter the setup for VNA-FMR experiments will be introduced. The original setup could perform FMR experiments in a cryogenic vessel, but for the purposes of this project multiple additions had to be made, which will be discussed in later chapters.

3.1 Insert with Co-planar Waveguide

The insert on which the waveguide is fastened consists of an RVS rod with heat shielding plates along its length. At the end a solid copper block is screwed with brackets for a waveguide and supports for a sample holder as can be seen in Figure 3.1. Through the insert run semi-rigid RF cables with SMA connectors on both sides. One cable is connected directly to the SMA connector on the waveguide and one cable is looped underneath the copper block and connected with 2 90-degree male-female SMA connectors unto the waveguide. At the head of the insert, the semi-rigid cables are connected to additional connectors for outside interfacing. The VNA that was used is a Rhode&Schwarz 14GHz VNA with N-type connections. This means the cables connecting the insert to the VNA are either N-type to SMA or require a N-type to SMA converter to interface the VNA. N-type and SMA connectors are accurate for applications up to 11GHz and 12GHz, respectively, but this can be increase to 18GHz in air dielectric connectors [18]. These connectors commonly use the 50 ohm impedance standard.
The waveguide on which our samples are placed is an open co-planar waveguide. It consists of two main conductive lines to carry EM waves: the signal line and ground planes. The CPW that was used is a double-

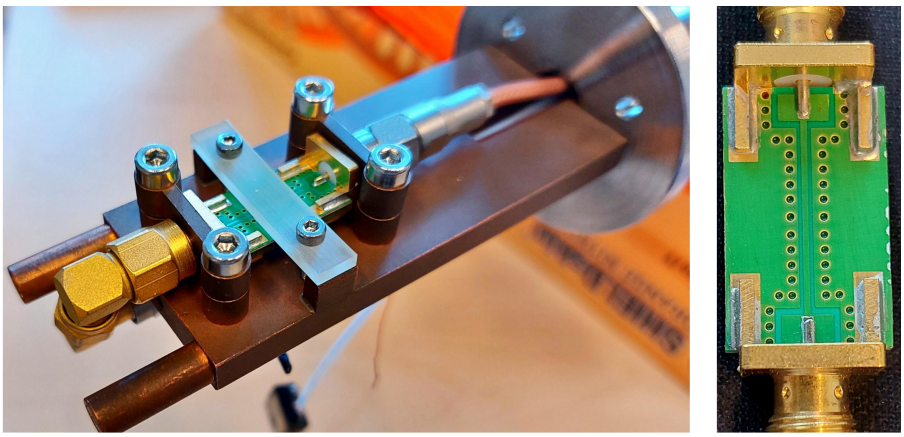

Figure 3.1: *Top down view of the waveguide and RF components at the end of the insert.*

layer PCB with the dielectric layer fully contained within the ground plane. There's coupling between the signal line and the ground plane on both the sides and the bottom of the CPW. This type of CPW is simply called a grounded coplanar waveguide (GCPW) in which the bottom ground layer helps confine the EM waves by limiting parallel modes [7]. CPWs can be designed to fit specific needs through tailoring their complex impedance and are often easy to manufacture. A change in impedance of the CPW can lead to reflections at the connecting interfaces. These reflections not only reduce the effective field strength through the CPW but can also cause frequency-dependent interference in response or reflection measurements. Schematic 3.2 shows the way a CPW can be represented electronically. A sample coupling to the CPW would show a change in inductive coupling constant C. The characteristic impedance of a waveguide system can be calculated with the following expression:

$$Z_0 = \frac{R + iwL}{G + iwC}. \tag{3.1}$$

Commonly, all applications are designed with a 50 ohm impedance to minimize impedance mismatch. As long as samples placed on the stripline are of similar material, size and placement, their local field strength coupling can be assumed to be the same. A waveguide and sample not designed with a specific coupling factor in mind, however, will result in impedance mismatch between the connectors and the waveguide.
The insert also contains a 4-point Cernox resistance sensor for temperature readout via a lock-in amplifier. For quicker recovery after a cryogenic mea-

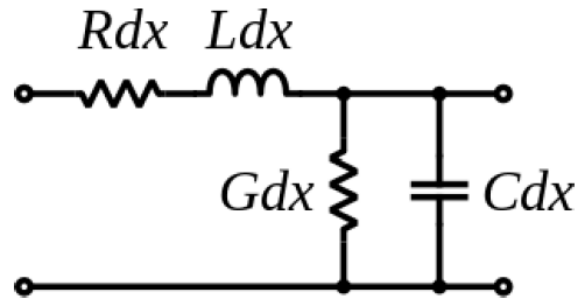

Figure 3.2: *Electronic representation of the waveguide-sample system, where the length of transmission wire dx is defined by resistance R and inductance L. The conductance of the waveguide is given by G and the sample is represented by the coupling constant C. Borrowed from De Haan(2019) [7]*

surement, a heating element is added. All connecting wires are soldered to a MIL spec connector to be interfaced with outside the insert. This connects to a custom breakout box. Exact details of the equipment used can be found in Appendix A.

3.2 Characteristic Response Insert

Before any FMR spectra can be measured, it is important to characterize the way RF signals are transmitted through the setup. Dissipation and reflections through the cables and connectors are unavoidable. This loss of signal will ultimately reduce both the amplitude of the driving field experienced by the sample and the return signal measured. Because smaller wavelengths have more opportunities of scattering through the setup, it is common to see the transmission signal decline with increasing frequency. Any significant dips at specific frequencies can indicate lossy connections or faulty cables. This was used to select RF-parts with the least overall loss and stable frequency response. There was access to 3 different sets of semi-flexible RF-cables that connect the insert to the VNA. The full spectra of the final insert with different sets of cables are plotted in Figure 3.3. As explained in section 3.3, VNA measurements express the signal loss in terms of the S_{21} parameter. We will analyze only the magnitude of this signal (expressed in decibels) and leave phase rotational data outside of our analysis. The difference in transmission of the different cables is largely due to their quality and length. Minimizing this length is a direct way to improving the transmission. The relatively short blue cables to the VNA ($<$1m length) also have the smallest periodic noise characteristic. Periodic

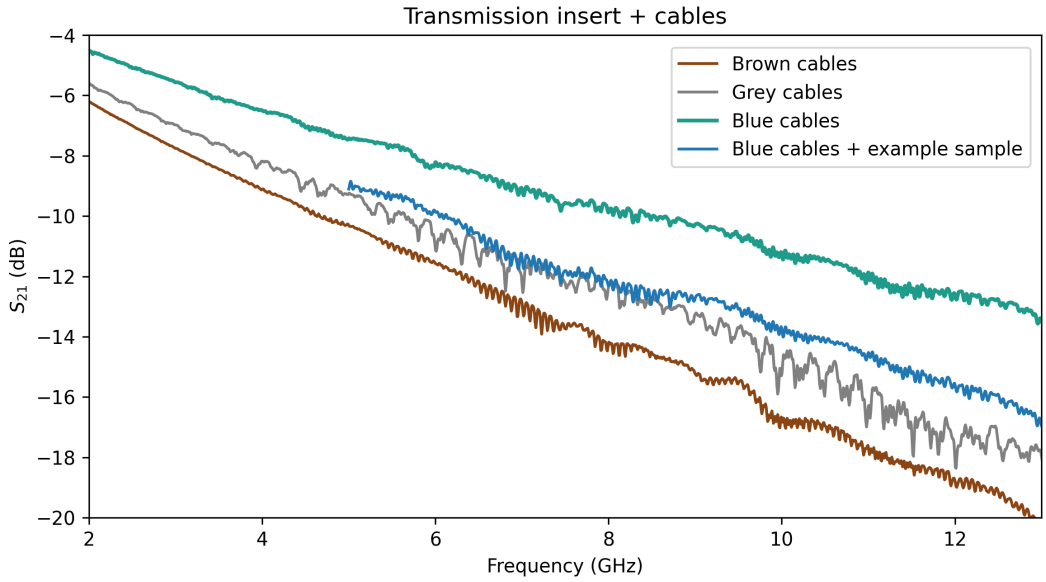

Figure 3.3: *Full cycle transmission through the insert and connecting cables as measured by a VNA for a wide range of frequencies. The waveguide did not contain a sample for the spectra used to measure the connecting cables. A sample of Co(30nm)Nb(30)Pt(5nm) was placed on the waveguide for the example sample measurement*

patterns are often caused by small damages inside the cable that accumulate over extended use. Sticking with the blue cables, the insert performs exceptionally well with full cycle loss of -11dB at 10 GHz. Compared to De Haan [7] and Van Dinter [21], who achieved -20dB and -13dB at 10Ghz respectively. This will ensure we lose as little signal as possible in our FMR measurements. The addition of an FMR sample also greatly influences the transmission. This is in part because the sample absorbs and dissipates some of the signal. Additionally, the sample changes the impedance of the waveguide to the connecting wires, increasing reflection of the signal. This makes the background transmission partly dependent on the type of sample used.

3.3 Sample Preparation

A large range of samples was prepared for the spectrum measurements. As a base, 300nm of oxidized silicon substrate was used. Each sample was cut to be roughly the same dimension of 8mm by 3mm with an estimated 10% margin between samples. This gives the samples after deposition of

a ferromagnetic layer a preferential magnetization axis along its long side. For the ferromagnetic layers, cobalt was readily available and easy to work with. Creating a thicker cobalt layer increases the magnitude of absorption, which makes it easier to detect in FMR measurements. However, due to the limited availability of cobalt it was determined to use 30nm Co as a sufficient FM layer. This was deposited, as are all other layers, by means of e-beam evaporation. The exact parameters of which can be found in Appendix B. For the normal metallic and superconducting layer, niobium was used. Above its critical temperature niobium functions as a normal metal with an effective spin diffusion length of 35-45nm [8]. Below T_c, niobium is a superconductor with a coherence length on the order of 18nm at T=4K. This was derived from the zero-temperature length by Jeon et al.(2018 supplementary), in other words a 'dirty limit' coherence length [11]. To confidently show the shift from spin diffusion length to coherence length as the dominant exchange distance below Tc, a gradient of sample thicknesses was used. These niobium thicknesses range from 10nm Nb to 50nm Nb in steps of 10nm, all preceded by a 30nm cobalt layer. To probe the exact length of the coherence length in niobium, each of these samples was made with a counterpart containing a Pt(5nm) capping layer. There is evidence platinum has special surface interactions with superconducting niobium. To compensate for these alterations to the surface dynamics inside the superconductor we can test the samples with a lesser spin sink capping layer. So lastly, to examine the spin sink characteristics of the Platinum, a third set of samples could be made with a copper or aluminum capping layer as applied by Louis2016 [14], which have relatively low SOC, making it a bad spin sink material. [10] The critical temperature of bulk niobium is generally taken to be T_c=9.2K. For thin films the superconducting transition is suppressed and Tc lowers as thicknesses decrease. As the temperature for resistance measurements does not decrease below 4.2K, it becomes increasingly harder to find Tc for t_{Nb}<10nm [20]. For several samples the Tc was measured and taken as the halfway point of the transition in the resistance. No superconducting transition was found for the Co(30nm)Nb(10nm) sample.

Chapter 4

Room Temperature Ferromagnetic Resonance

Aside from supplying our dynamic system with a microwave driving field, an external constant field is needed to influence the resonance frequency. In this section we'll examine a basic way of generating (homogeneous) external magnetic fields. We will use this to measure and analyze our first set of ferromagnetic resonance spectra at room temperature.

4.1 Initial Testing

A simple way to supply an external field is by using permanent magnets. Neodymium magnets are especially useful for tabletop measurement as they are strong and come in many different shapes. A square magnet of 10x10x5 mm was used for preliminary testing. Naturally, the beginning of any project involves familiarizing oneself with new equipment and measurement techniques. For sake of brevity, a large portion of trial and error will not be discussed. However, this initial period can be summarized into a single lesson: to prioritize real time feedback as a diagnostic tool. Once the VNA was not only used for data acquisition, but its internal analytics were used to show FMR resonance spectra in real time, significant progress began to be made.
For the first full spectrum measurement a sample of Co(30nm)Nb(30nm)Pt(5nm) was evaporated on 300nm silicon substrate. Even though this is not a simple bulk ferromagnet, at room temperature this sample can be considered as a ferromagnet and normal metal heterostructure. This should not affect the ferromagnetic resonance spectrum in a meaningful way. The sample

is placed face down onto the center trace of the waveguide and secured with a plastic sample holder. To control the height of the magnet (and the field strength) the magnet was attached to a ruler held above the waveguide by a tabletop jack. For each measurement the zero-field background spectrum is subtracted from the resonance spectrum. The combined spectra are plotted in Figure 4.1a. It should be noted that al spectra have been smoothened with a 4% rolling average window (depending on resolution this comes down to 30MHz). The FMR absorption dips are clearly visible in the spectra. However, at higher resonance frequencies the spectrum drifts from the baseline and the absorption loses shape. These distortions increase drastically whenever an object enters within a 10mm radius of the open waveguide. Likely, this is caused by inductive coupling between the RF signal leaking from the waveguide into the surrounding free space and any object therein. This leads to an impedance mismatch between the waveguide and the SMA connectors on the RF cables. To test this, the same configuration was measured with a non-ferromagnetic silicon substrate sample, which is shown in Figure 4.2. This clearly excludes the sample as a source of these distortions and we can use the substrate measurement to clean our initial spectrum measurement, shown in Figure 4.1b.

4.2 Permanent Magnets

Although the $\leq$6GHz resonances are clear, the distortion still affects higher resonance frequencies. To improve on the uniformity and strength of the external field, differently shaped magnets were tested. It was expected that cylinder bar magnets could improve field uniformity over the square magnets, because the square magnets have cornered edges. By stacking multiple square magnets we can increase the field strength over a single magnet. Figure 4.3a was obtained by using a handheld gaussmeter. The cylindrical bar magnets produce insufficient field and have increased distortion at higher frequency resonance as seen in Figure 4.3b. We see a normal FMR spectrum around 4GHz, but this is overshadowed by the volatility above 7GHz. This is likely caused by the bars extending over de connections to the waveguide due to their size. It seems the SMA-connectors contribute more to the leaking RF-fields than the waveguide itself. The best result was obtained by using a stack of 3 square magnets. The output field can be increased significantly while staying a safe distance from inductively coupling to RF-components and will be applied for all RT FMR measurements from here on.

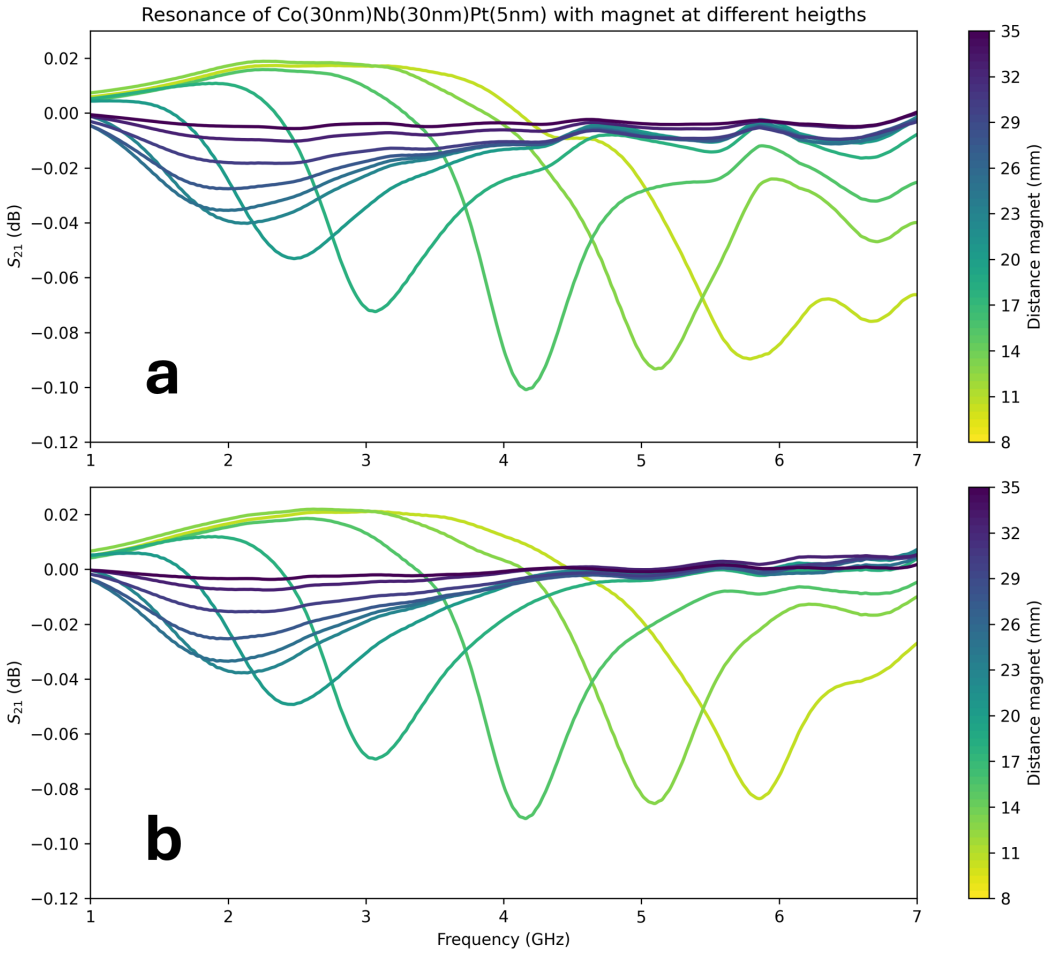

Figure 4.1: ***a*** *RT FMR spectra of Co(30nm)Nb(30nm)Pt(5nm) thin film for a permanent magnet at varying heights supplying in plane external field.* ***b*** *The same FMR spectra after subtraction of the response from a non-ferromagnetic sample under similar measurement.*

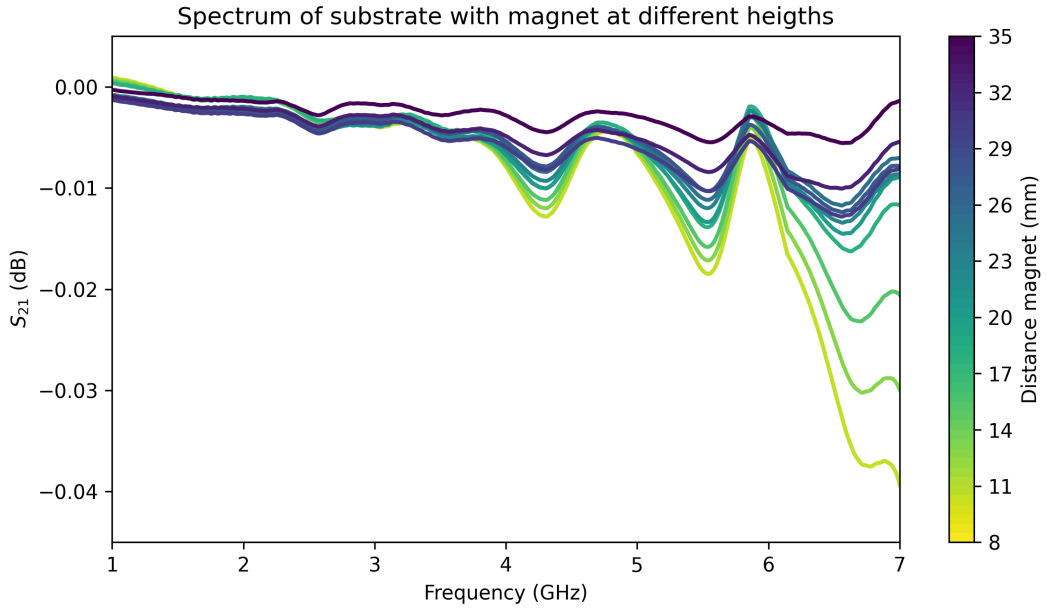

Figure 4.2: *RT Spectrum of non-ferromagnetic substrate sample for a permanent magnet at varying heights supplying in plane external field.*

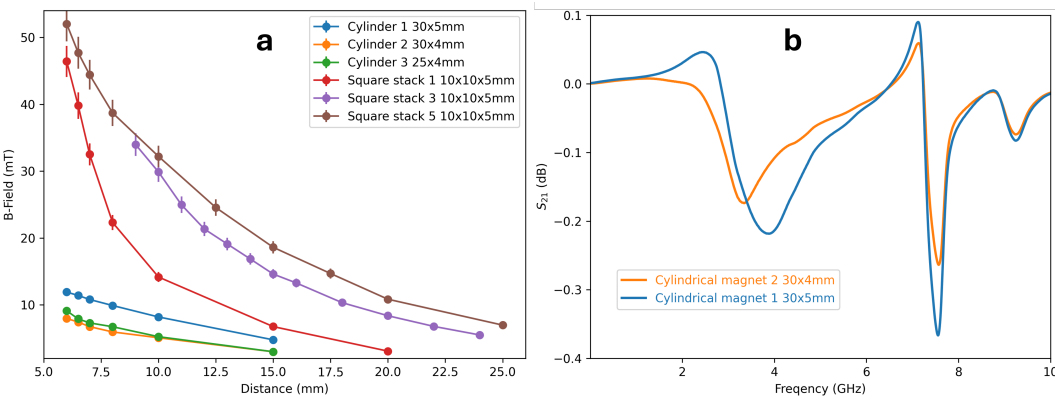

Figure 4.3: ***a*** *Magnetic field strength as measured by gaussmeter for different shapes of neodymium magnets at varying distance from the magnet.* ***b*** *RT FMR spectra of Co(50nm)Nb(20nm) when supplied with an in plane external field from two different cylindrical bar magnets held at 8mm from the waveguide.*

4.3 Effective Magnetization

An easy-to-overlook component of FMR experiments is the discrepancy between the applied field and the internal field experienced by the ferromagnet. By increasing the external field we can align the internal magnetic moments inside the ferromagnet and saturate it up to the saturation magnetization M_s. Changes in this material dependant quantity can shift the resonance frequencies and the magnitude of the RF signal absorption. One factor affecting M_s is the thin film anisotropy. Local differences in crystal structure, the macroscopic shape of the thin film and surface interactions contribute to the total anisotropy of the sample, which works to resist alignment of the magnetic moments. We will model this as a single factor adjustment K to M_s and define an effective magnetization M_eff:

$$M_{eff} = M_s - \frac{2K}{M_s} \tag{4.1}$$

The relationship between resonance frequency and the external field is nicely described by the Kittel formula. It is derived from 2.2 in absence of damping:

$$f_{Kittel} = \frac{\gamma}{2\pi}\sqrt{H_{ext}(H_{ext} + \mu_0 M_eff)} \tag{4.2}$$

Where the gyromagnetic ratio γ is given by:

$$\gamma = \frac{g\mu_B}{\hbar} \tag{4.3}$$

By taking the resonance frequencies and field strengths of the previous section, the Kittel formula can be fitted and compared to expected values for our thin film samples. Aside from the saturation magnetization, the Kittel formula depends largely on the Landé g-factor, which linearly decides the gyromagnetic ratio γ. Prior research repeatedly shows the g-factor to be thickness dependent [9]. In this case, we set g = 2.10 for 30nm of cobalt and M_s = 1.44e6 A/m.
The fit for Co(30nm)Nb(30nm)Pt(5nm) in Figure 4.4a shows a high value for the effective field equal to 1.66 T. It is close to the theoretical saturation magnetization and differs only by roughly 8%. The same process was undertaken for a thin film sample of evaporated Co(30nm)Nb(20nm) as shown in Figure 4.4b. A very similar result was found with an effective field of 1.72 T.
Although these values differ significantly from similar applications such as Jeon et al.(2018), who found between 0.78 and 0.88T for 6nm permalloy in a niobium stack, and Chen et al.(2007) who found 1.01 to 1.36T

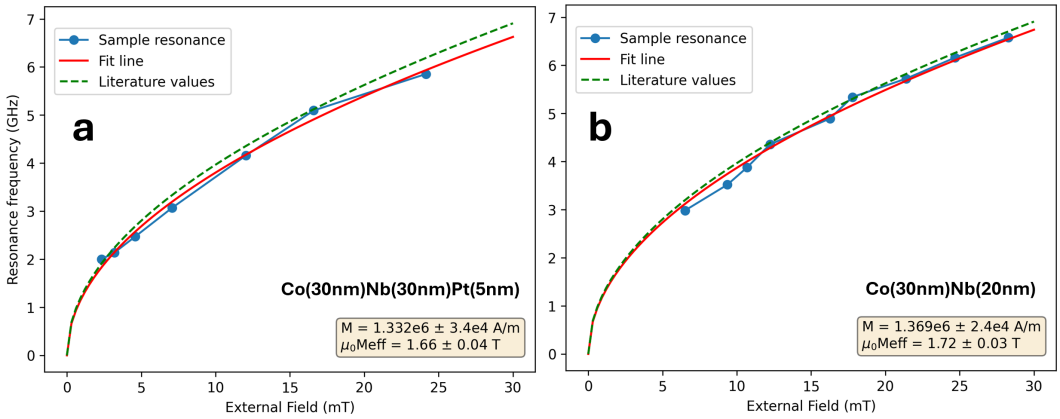

Figure 4.4: ***a*** *RT Resonance frequencies of Co(30nm)Nb(30nm)Pt(5nm) thin film on Si thermal oxide substrate with kittel formula fit in red. The fitting formula used is* $f_{Kittel} = \frac{\gamma}{2\pi}\sqrt{H_{ext}(H_{ext}+\mu_0 M)}$*. The resulting effective magnetization is shown in the bottom right corner. The literature values mentioned in the text are plotted as the green dashed line following the kittel equation.* ***b*** *Similarly, the resonance frequencies for Co(30nm)Nb(20nm) are fitted to the kittel formula.*

for 30 to 360nm permalloy respectively. A precedent for anomalous effective field in evaporated permalloy with CPW-FMR has been found by De Haan(2019), who comments that the empirical values seem off by a factor of 2 compared to his 1.0T assumption.
For the application of Cobalt, an explanation is presented by Beaujour et al.(2006) [1], who proposes that the g-factor in cobalt thin films is significantly higher in application than in theory for fcc Co films. In his analysis of sputtered and evaporated thin films, an exceptional increase in g-factor is found especially for the evaporated films, which differ by 16% up to $g = 2.49$. The resulting effective magnetization shows an increasing trend with ferromagnet thickness, leading to very similar values as found here.

Having established a methodology for room temperature FMR measurements, the conditions to apply this technique at low temperatures are almost met. Before the next step, a few alterations were made. First of which concern the generation of external magnetic fields in situ, as the permanent magnets used at RT are too large and impractical to use inside a cryogenic vessel.

Chapter 5

Superconducting Coil Design

The goal is to create a way of generating variable magnetic fields in a confined cryogenic system. Most commonly, cryo-magnetic measurements are done using a vector magnet system integrated in the cryogenic vessel that can supply an external field from a distance. For use in an unaltered cryogenic vessel, a stand-alone coil wound with superconducting wire was made, which can be attached locally to the insert. The absence of resistance in a superconducting coil below its critical temperature makes achieving higher field strengths easier and annihilates heat generation from powering the field compared to non-SC coils.

5.1 Field Strength

The resonance frequencies at which the system can be measured are first and foremost determined by the strength of the external field. From the Kittel formula we can estimate the necessary strength to measure up to 8GHz resonance to be 60mT. In general, a Helmholtz configuration that makes use of two identical coils is preferred for applications where the uniformity of the field is of great importance. For reasons that'll be elaborated later, we'll instead focus on designing the coil as a single cylinder. The following formula determines the field strength at the centre of a finite coil where the radius to centre is larger than the width of the coil:

$$B(T) = \frac{\mu_0 NI}{2R} \tag{5.1}$$

The number of wire windings N, the current I and the radius R will greatly inform our designing process.

5.2 Practical Considerations

The strongest limitation we have to consider is that the radial size of the coil must be smaller than the entry of our cryogenic vessel. For a standard cryogenic vessel this comes down to less than 50mm. The width cannot be larger than the 18mm waveguide due to the distortions caused by lossy connectors mentioned in Section 5.2. These considerations together limit the number of windings of wire we can loop around our coil base. That leaves one last knob to turn to control the output field of our coil: The current. Keeping in mind inefficiencies in the final coil, using currents on the order of 1A should suffice.
The coil base was milled out of PEEK (Polyether Ether Ketone), which has great thermally insulating properties and is resistant against cryogenic temperatures. The walls of the coil base are only 0.5mm thick, which for a thermoplastic like PEEK makes it prone to breaking at the edge. By filling the coil base with wire, we provide support and reduce its fragility.
As a proof of concept, a coil with 120 windings of 0.11mm diameter Cu-coated NbTi wire was wound. This coil has a room temperature resistance of 74 ohms. For a tabletop field measurement, we use a probe-type gaussmeter. Naturally, we are interested in the field through the center of the coil, but due to the measurement surface lying parallel to the probe, measurements could only be taken outside the coil base as seen in Figure 5.1a. It averaged 0.26mT per 0.1A of current. This is only 58% of the expected output.
Due to shortage of wire, the final coil has 2600 windings of a different 0.12mm diameter Cu-coated NbTi wire. For this, roughly 340 meters of wire was used. The final characteristics of the coil are summarized in Table 5.2. This coil has a room temperature output of 6mT per 0.1A. This is 73% of the calculated value and should suffice for our goals. The nature of our experiment requires regularly interchanging the sample on the waveguide. The coil, which fully encompasses the waveguide, must easily be removed and reconnected. To do this, pin connectors were added to the inside of the coil base matching the pins soldered to the connecting wires, see Figure 5.1b. To hold the coil base in place, two L-brackets are used. These brackets are screwed onto the setup with spring sinkers to prevent loosening during thermal expansion. The area of the coil base in thermal contact with the rest of the setup is limited. The requirement of ease of use, together with size limitations, is what makes a Helmholtz coil setup impractical in this case.

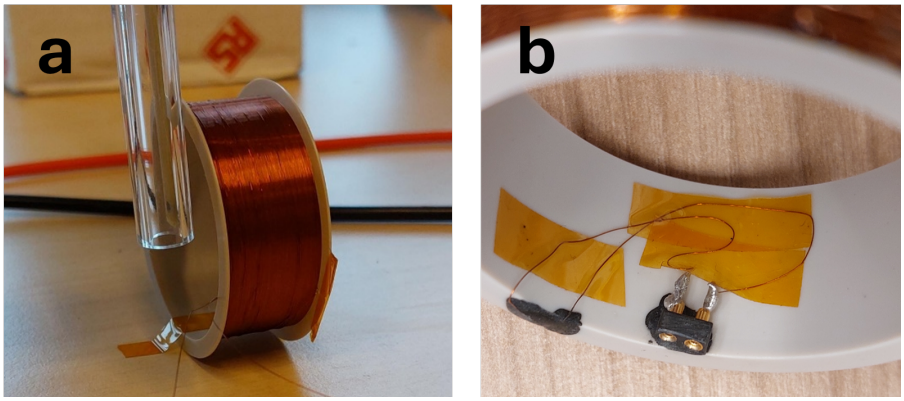

Figure 5.1: ***a*** *Initial N=120 coil with the hall probe held just outside the centre of the coil for field measurements.* ***b*** *Pin connectors attached to the inside of the N=2600 coil.*

Inner-outer diameter	Width	Wire type	Critical current wire	# windings	RT resistance	Inductance
42mm – 48mm	18mm	0.12mm Cu-coated NbTi	6.1A at 1T	2600	1291 Ohm	324mH at 1KHz

Figure 5.2: *Table of the defining characteristics of the final superconducting coil.*

5.3 Resistive Heating

The limit on the current through the coil is a lot lower than the theoretical limit of the NbTi-wire, at least if the temperature is to be controlled. Any low temperature measurement inside a cryogenic vessel comes with the practical concern of ohmic heating through the wires. Although the superconducting coil experiences very little heating, the connecting wires will mostly exist above the critical temperature for the wire. Estimating the heating can be difficult because the wire experiences a gradient of temperatures. If we assume simple copper wire of the same gauge as the NbTi, resistivity at an average low temperature and a max current of 1A we can estimate the total power through the wires as 4W. A good rule of thumb is that 1W for an hour will boil away a liter of liquid helium*. Fortunately, there's a simple trick we can apply. By dividing the connecting wires into multiple parallel bundles we distribute the current over many paths, decreasing the current per bundle. Practically, we have now increased the number of heating sources linearly, but because the power generated scales with I^2 we still reduce the heating output as shown in Equation 5.2.

*Back-of-the-napkin wisdom kindly provided by Tjerk Oosterkamp

For a 4 bundle setup for example, the power output is reduced by $\frac{1}{4}$. The same can be achieved by simply using a thicker wire to reduce the resistance, but we're limited by a single gauge of superconducting wire.

$$P(W) = RI^2 = \frac{\rho L n}{\pi r^2}\left(\frac{I}{n}\right)^2 \tag{5.2}$$

With n the number of wires, ρ the resistivity, L the length and r the radius of the wire. Lastly, there's the possibility of the coil losing superconductivity. This can happen as either the helium boils away too far to keep the coil cool or the coil experiences more than its critical magnetic field. As the field strength produced by the coil for AC current is dependent on the change in current, it is possible for the coil to lose superconductivity when the input current is abruptly stopped. In which case, the coil discharges its full inductive energy capacity as heat. With Equation 5.3 We can estimate the energy capacity of the coil using the self-induction L. For a 1A scenario this gives roughly 0.16 Joules of energy. Even if we assume the energy dissipates over several seconds, this still proves a danger as liquid helium expands to 200 times its volume just above its boiling temperature. For this reason, all cryogenic vessels are equipped with safety pressure valves.

$$E_{ind} = \frac{LI^2}{2} \tag{5.3}$$

Two thermal anchors are added to contact the helium bath below the insert. The coil is finished with a layer of thermally conducting GE-varnish, which improves the thermal contact between the anchors and the coil. It also prevents damage to the wire during handling. The final dimensions of the coil only allow for 0.5mm margin with the width of the vessel, thereby maximizing the available space.

5.4 Field Matching and Results

To assess the generated field created by the coil in situ, a Hall probe could be used. Although probes exist that can measure broad ranges and operate at cryogenic temperatures, they are hard to come by and require significant investment. The relation between supplied current and field output of the SC coil was obtained with a different approach. The low temperature resonance frequencies with the supplied current were taken and compared to RT resonances obtained using a permanent magnet with known field strength. Essentially, the coil output was mapped onto a kittel

Initial Temperature (K)	Coil current (A)	Increase in T (K/s)
< 10	0.2	Negligible
< 10	0.4	Negligible
15	0.2	0.08
15	0.4	0.25
20	0.2	0.2
20	0.4	0.6

Figure 5.3: *Table showing the heating per second as measure by the cernox thermometer for different input currents and initial temperatures.*

relation obtained at RT. This was done for a sample of Co(30nm)Nb(20nm) using spectra measured at 0.2, 0.25, 0.3, 0.35 and 0.4A at T=9K. From this, a simple conversion factor α was found. The ferromagnetic properties of the sample change between RT and cryogenic temperatures. So does the saturation magnetization, which prevents a true mapping of resonance frequencies. Regardless, precise determination of field output is not essential for determining peak broadening in the FMR spectra.

$$B_{coil} = \alpha I \tag{5.4}$$

$$\alpha = 63.8 \pm 0.14 \, \frac{mT}{A} \tag{5.5}$$

During these calibration measurements an oversight in the design of the coil was found. For measurements at T$\leq$10K, the thermal contact with the helium bath is strong and fluctuations in the temperature are negligible. At higher initial temperatures the thermal contact is less good and a steady increase in temperature is seen during measurement sweeps (which usually takes 20-25 seconds total). By examining later measurements, an indication of the temperature increase per second can be given. From Table 5.3 It is clear that the heating is significant and larger than could be caused by the connecting wires alone. The culprits are the soldered pin connectors as seen in Figure 5.1b These are high resistance compared to the superconducting wiring. Due to the placement of the Cernox thermometer on the bottom plane of the insert, directly opposite the pin connectors, it is possible the thermometer is overestimating the temperature increase of the sample. Regardless, by keeping the frequency span no larger than necessary the time to completion can be minimized without sacrificing measurement resolution.

Chapter 6

Cryogenic Resonance Spectra

In this chapter the first testing of the insert at temperatures below 20 Kelvin will be discussed. Complications arriving from the new environmental parameters will be examined and improvements on the methodology are implemented. Any adjustments in measurement goal are explained, which will prepare the discussion of the results of the cryogenic FMR measurements for thin film heterostructures.

6.1 Initial Testing

In line with previous testing, the first sample to be lowered into the cryostat was a Co(30nm)Nb(30nm)Pt(5nm) thin film sample. Between the liquid helium bath and the top of the vessel, a gradient of temperatures ranging from 4 to 150 Kelvin exists. The temperature at the waveguide on which the sample is placed, is controlled by changing the depth of the insert inside the cryostat. Spectra for two different field strengths were obtained and are shown in Figure 6.1a. The spectra clearly show a disruptive quantity of noise. As the helium bath absorbs heat and boils off, the vibrations from bubble nucleation affect the measured spectrum. Although the FMR absorption is still visible, the magnitude of the noise will worsen the determination of peak width. What's more, a sudden decrease in transmission at 6GHz is seen, likely caused by the VNA switching measurement modes between lower and higher RF frequencies during the sweep. This jump gets larger when the no-field baseline starts to drift away from the baseline measurement taken for normalisation as the temperature changes. To combat this problem, brushes were added to the thermal anchors of the coil and the lower end of the insert (Figure 6.1b).

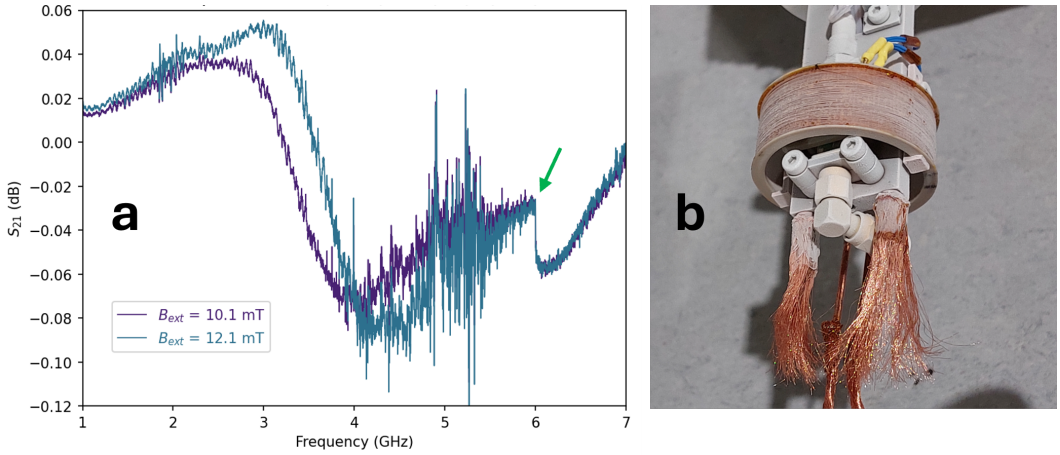

Figure 6.1: a *FMR resonance of Co(30nm)Nb(30nm)Pt(5nm) at T=9K for two different external field strengths. The green arrow marks the discontinuity in the spectrum.* ***b*** *The coil attached to the insert and the copper wire brushes attached to the copper block.*

These brushes dampen the vibrations extended through the anchors to the insert. Additionally, by committing to let the insert thermalise inside the vessel for 3 to 4 hours before measurement, temperature differences are allowed to equalize. Together, these interventions greatly improved the stability of later spectra. As explained in Section 3.4, the spin diffusion length in niobium is on the order of 35-45 nm. To identify an increased Gilbert damping upon introduction of a Pt capping layer, the Co(30nm)Nb(20nm) and Co(30nm)Nb(40nm) can be compared to their Pt(5nm) counterparts. For this reason, it was decided to start analytical measurements with the 20 and 40nm niobium samples.

6.2 Linewidth Results

The Co(30nm)Nb(40nm) sample has a T_c of 7.1K, the Co(30nm)Nb(20nm) sample a T_c of 6.5K. Spectra were obtained for a multitude of fields at different temperatures, the exact set of measurements can be found in Table 8.2. Additional information on the measurement parameters and data processing performed by the VNA can be found in Appendix C.
A subset of these measurements are shown in Figure 6.3. Two things are of note. Firstly, the high-field spectrum in Figure 6.3c does not follow the same trajectory of increasing magnitude as seen in the spectra obtained at T=5K. This is likely caused by the quick temperature rise that occurs when

powering the coil with lesser thermal contact as mentioned in section 5.4. This might skew the calculated peak width for this particular spectrum. Secondly, all spectra are asymmetrical in the sense that their response at low frequencies is higher than that at high frequencies. The difference being more than half the peak magnitude. Chen et al.(2007) [4] also notes asymmetrical absorption spectra for Permalloy (NiFe) films and proposes it results from impedance mismatch in the combined waveguide-sample system. To calibrate against this, phase rotation analysis could be performed, which is outside the scope of this project. Practically, the peak-to-peak width method utilising derivatives as described in section 2.4 seizes to be a good measure of peak width. Henceforth the linewidth will be examined using the 90-percent linewidth method as outlined in the same section. The extracted 90-percent peak linewidths are plotted in Figure

Co(30nm)Nb(40nm)		Co(30nm)Nb(20nm)	
Temperature (K)	**Field Strength (mT)**	**Temperature (K)**	**Field Strength (mT)**
9.5	11	20	12.9
5.7	12.4	5	16
5.1	15.3		19.1
4.5			22.3
			25.3

Figure 6.2: *Table showing the exact temperatures and external magnetic fields for which spectra were obtained for both the Co(30nm)Nb(40nm) and the Co(30nm)Nb(20nm) samples.*

6.4. To reiterate, it is expected for the linewidth to decrease past the transition temperature. More so for Nb(40nm) than for Nb(20nm). There appears to be a downward trend, but especially the linewidths for Nb(40nm) are inconsistent. To determine whether the results themselves are inconclusive or the measurement parameters could be tuned to improve the differentiation resolution, the findings from Jeon et al.(2018, supplementary) were consulted. Figure 6.5 shows the FMR linewidth for samples with different thicknesses of Nb. Each subfigure is comprised of 3 plots at different temperatures, one above T_c and two below. It is clear the linewidths above and below Tc diverge with increasing resonance frequency. The difference in linewidth around 4-6GHz is marginal, practically indistinguishable for $t_N b$ = 30nm. If we analyse the $t_N b$ = 15nm and $t_N b$ = 45nm plot around 5Ghz for example, we can estimate the field linewidth broadening is 0.05mT and 0.2mT respectively. With help of

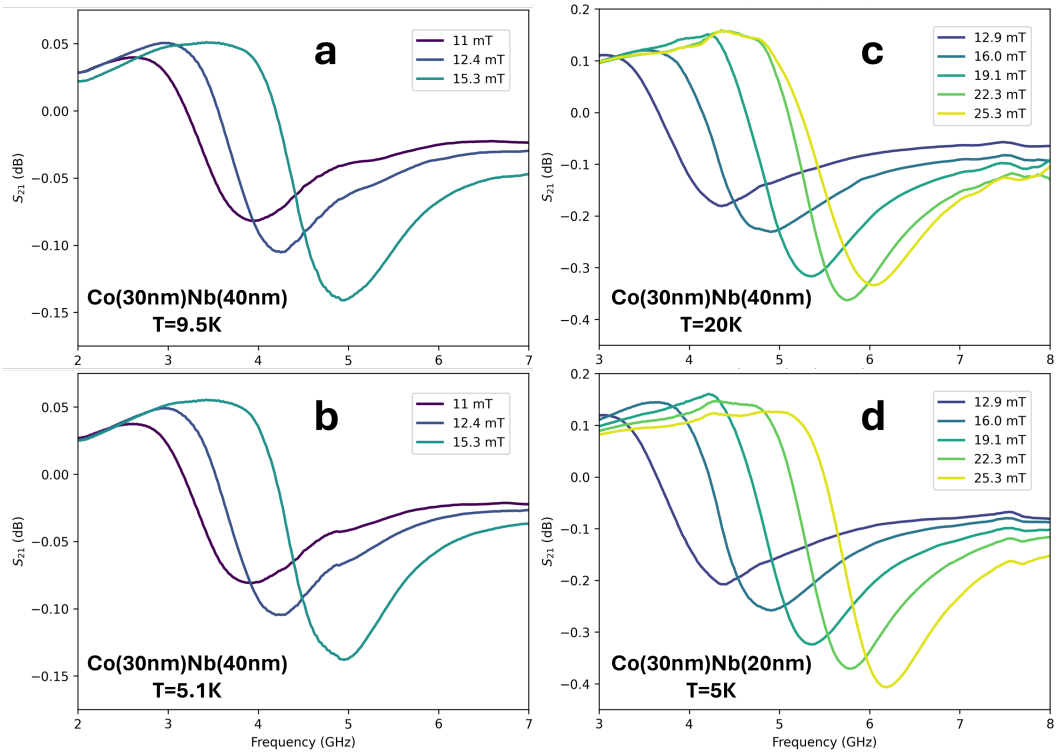

Figure 6.3: *A subset of obtained FMR resonance spectra above and below T_c for different external field strengths. It shows Co(30nm)Nb(40nm) at* ***a*** *T=9.5K and* ***b*** *T=5.1K. Similarly for Co(30nm)Nb(20nm) at* ***c*** *T=20K and* ***d*** *T=5K.*

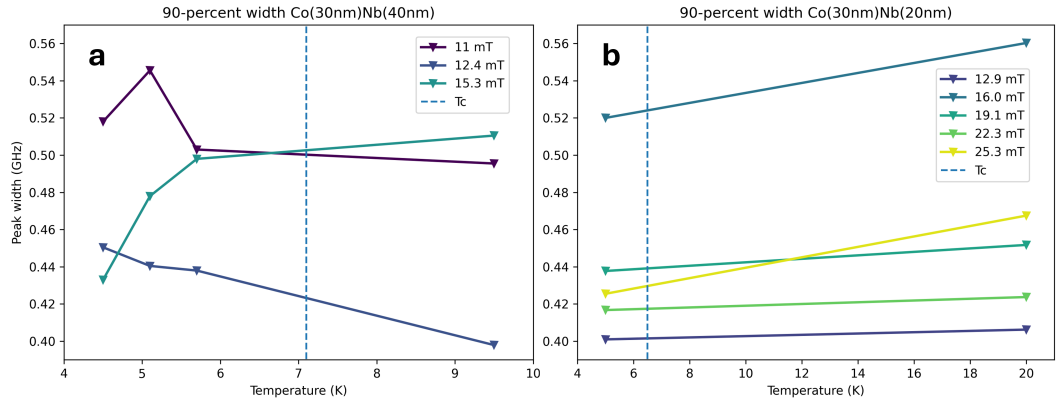

Figure 6.4: ***a*** *90-percent resonance linewidths as a funtion of temperature for the full measurement set of Co(30nm)Nb(40nm). The dashed line shows the T_c of the sample.* ***b*** *similarly for the measurement set of Co(30nm)Nb(20nm)*

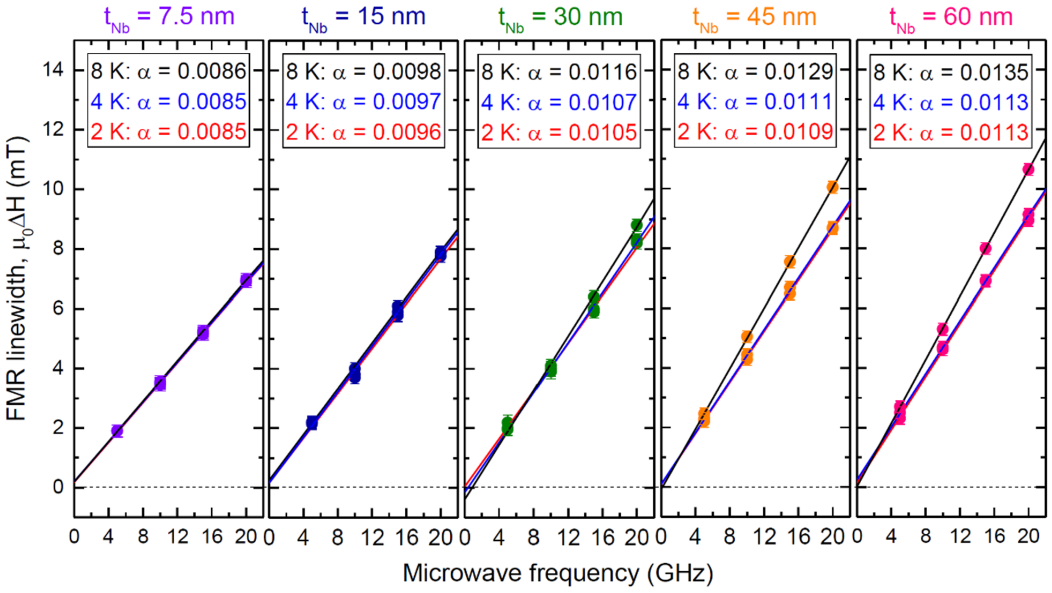

Figure 6.5: *FMR linewidth as a function of frequency f from FMR spectra of Nb/Py/Nb at T = 2, 4 and 8K. The solid line are fitting curves used to deduce the Gilbert damping constant α. Borrowed from Jeon et al.(2018, supplementary) [10].*

Kalarickal et al.(2006) we can estimate this to correspond to 8MHz and 30MHz of frequency linewidth broadening, well within the measurement resolution of the datasets. Another difference is that Jeon et al. finds the linewidth to increase linearly with increasing resonance frequency, whereas our samples neither show such a relation. It is clear that the discernability of a shift occurring around T_c improves at higher resonance frequencies. Minding the biggest limitations of the setup, both in the impedance matching of the waveguide and the heating of the coil at higher power, it is preferred to obtain future measurements at higher resonance frequencies, with a rough limit of approximately 8GHz resonance.
It was decided to test the Co(30nm)Nb(20nm)Pt(5nm) and Co(30nm)Nb(40nm)Pt(5nm) samples before returning to the no capping layer samples to extend their datapoints. During measurements however, the baseline transmission of the insert kept changing erratically and below T=8K no FMR absorption was seen. The FMR spectra above this temperature were of lesser magnitude and contained more distortions. Upon inspection of the spectra without subtraction of a baseline the difference becomes more apparent (Figure 6.6). The previous measurements had an average background transmission of roughly -14dB and attenuation declined slightly as the tempera-

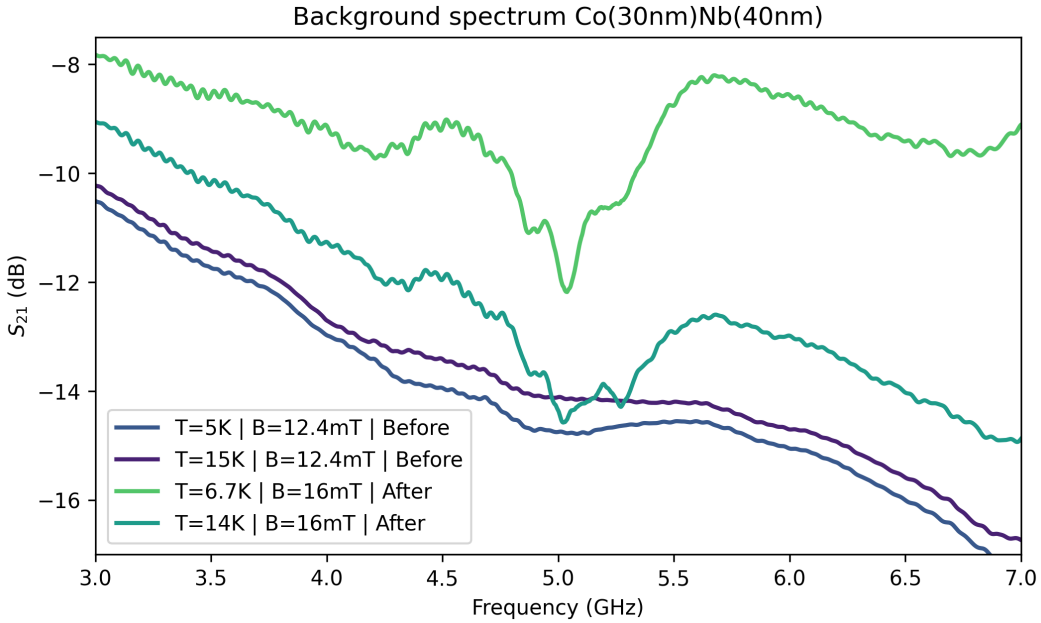

Figure 6.6: *The baseline transmission through the insert with Co(30nm)Nb(40nm) sample, similar to Figure 3.3. Taken before and after the insert was compromised, at different temperatures and external field strengths.*

ture decreased further. In the current situation, the base transmission is higher than previous and there are distortions visible around 5GHz. As the temperature drops the background transmission of the insert rapidly increases.
Changing samples, VNA measurement modes and interchanging the RF-connectors on the insert yielded no improvement. One possible explanation is that the waveguide connections were damaged during the measurement cycles. During warmup outside the vessel ice accumulates on the insert, sublimating from the surrounding air. If the insert is not sufficiently dried before the next cooldown, water can freeze and break the sensitive equipment. As the compromised insert prevented adequate measurement below the T_c of all samples, it was decided to only take additional above T_c measurements for the Co(30nm)Nb(20nm) and Co(30nm)Nb(40nm) samples to improve the existing results. The combined results with are shown in Figure 6.7 and Figure 6.8.
The linewidth for Co(30nm)Nb(40nm) is highly inconsistent between the older and newer measurements and were therefore not plotted continuously. Frustratingly, a piece of the sample broke off in between the two sets of measurements, shortening it by about 1/3rd. This should not af-

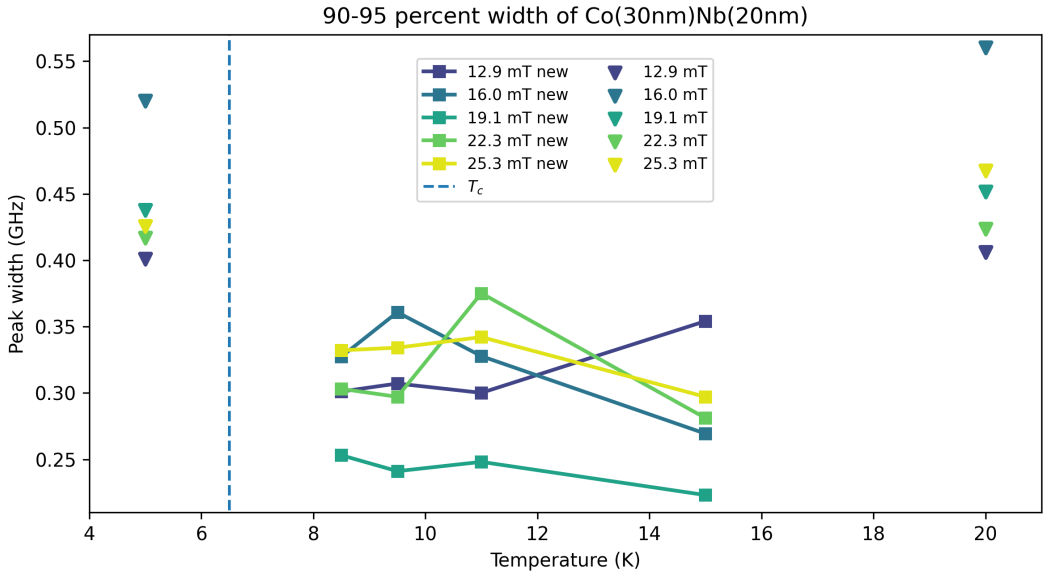

Figure 6.7: *Temperature dependence of the FMR 90-percent linewidth of Co(30nm)Nb(20nm) for different resonance fields. The square markers indicate the added measurements and the triangle markers previous results. The dashed line indicates T_c.*

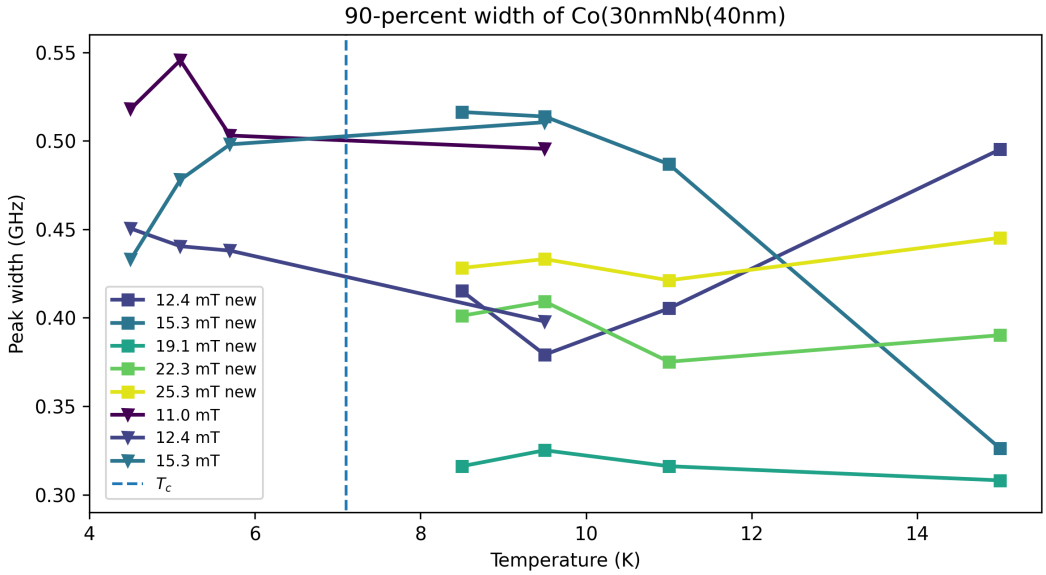

Figure 6.8: *Temperature dependence of the FMR 90-percent linewidth of Co(30nm)Nb(40nm) for different resonance fields. The square markers indicate the added measurements and the triangle markers previous results. The dashed line indicates T_c.*

fect the damping characteristics and linewidth in an absolute sense, but it can decrease the magnitude of the absorption spectrum. As we're using a non-standard definition of linewidth, it's dependent on absorption magnitude in a way a FWHM-linewidth would not be. It's fairly certain that this linewidth shift is not the result the problems with the insert, as the newer linewidths for Co(30nm)Nb(40nm) coincide with the older results. Only two points were doubly measured: 12.4mT and 15.3mT at 9.5K. 15.3mT falls in nicely and the 12.4mT datapoint differs by roughly 10%. There is a possibility for a high reproducibility error, but there are too few repeated measurements to draw conclusions.
With the limited results available, it cannot be concluded that the data show a decrease in linewidth below T_c. It also does not show the same linear increase in linewidth with increasing resonance frequency as found by others. If there is a decrease in linewidth present in the data it is smaller than the error introduced in the analysis method. Based on the uncertainty in the data, no conclusive comparison can be made.

Chapter 7

Conclusion and Outlook

To summarize, a lot of work was done to create a method to simplify research into the interesting field of long-range spin triplet superconductivity. In the end, a low loss method of performing FMR measurements was presented. The full system has a -1dB per GHz attenuation and it outperforms many other open coupled RF systems. It has been used to reliably measure FMR spectra and can be used on many different sample compositions. Multiple different thin film heterostructure sample sets were created with Cobalt-niobium FM-SC interfaces. For the low temperature measurements, a superconducting coil was designed with many practical considerations and an 80mT local field limit in mind. The coil produces consistent, homogeneous magnetic fields locally. A subset of samples has been analysed measured at resonance frequencies between 1GHz and 6.5GHz at both room temperature and cryogenic temperatures as low as 4.5K. The results showed consistent, although asymmetrical FMR spectra. The linewidths could not reliably be determined using conventional methods. However, a small decline in linewidth below Tc was noted using a custom definition of linewidth. This would indicate a decreased Gilbert damping coefficient for Ferromagnet-Superconductor heterostructures. Unfortunately, the project was cut short due to complications with the insert. Unused sample sets entice further research and with a few recommendations, the full potential of the setup can be explored.
For more pronounced linewidth shifting, it is essential to measure at higher resonance frequencies. At least $\geq$10GHz resonance, but 20GHz is most common. The coil was designed to be capable of producing higher output fields. These would be able to induce 12GHz resonance and potentially even higher resonances. The heating produced by the pin connectors puts a limit on this and could be unlocked by redesigning the connection to

the coil. Unfortunately, the insert suffered from distortions at these higher frequencies. Most SMA and N-type connectors degrade quickly and are rated for only 500 matings. As wear increases the maximum operating frequency decreases. The VNA's converters and cables we're relatively new, but the insert RF-cables and the waveguide with its connectors had an unknown amount of previous use. It is likely that the inability to prevent distortion of the spectra at frequencies above 7GHZ is the result of degradation of the SMA connectors on the insert. It is recommended to replace these RF components and to design an open waveguide whose impedance matching profile is determined with the coupling of a thin film sample in mind. Analytically, the spectra could be improved by utilizing phase data and applying sloped attenuation power to combat frequency dependent losses. By repeating measurements, datapoints can be better differentiated and a sense of the accuracy in the determination of linewidth can be obtained.
Multiple lines of inquiry remain open and could lead to interesting results. First and foremost, the setup can be used for the detection of increased damping when a strong spin sink capping layer is added to F-SC multilayers. Additionally, the effect of SOC characteristics of the dissipation of long-range spin triplets could be explored by using different materials as a capping layer, such as Au and Cu in comparison with Pt. Lastly, many exotic superconducting materials could be tested on their ability to generate triplet states in adjacent ferromagnetic layers. With protocols informed by the previous findings, more could be learned about the type of superconductivity in unconventional superconductors such as LSMO.

Acknowledgements

I would very happily take this chance to thank everyone involved in realising this project with me. First and foremost I would like to thank Kaveh Lahabi for the opportunity to start this project. His ability to inspire and transfer his enthusiasm has motivated me and many others on our path through the chaotic world of physics. Secondly, Tycho Blom for supervision, support and the many conversations that have given me perspective, both in matters of research and personal matters. Matthijs Rog I would like to thank for his technical expertise and his assistance at moments most critical to this project. Many thanks to Jan Aarts for his enticing questions during group meetings and offering to be second corrector. Lastly, Harry Visser from the electronics department for letting me borrow equipment many times over. Naturally, there were many others who I was blessed to meet and befriend. I am very thankful for the opportunity and the many things I have come to learn over the course of this project.

Chapter 8

Appendices

8.1 A: Equipment Details

The following is a non-exhaustive list of the equipment used in the setup.

- **VNA** = Rhode&Schwarz ZNLE14 2-port Vector Network Analyzer
- **Blue Cables** = Rhode&Schwarz 50cm SMA-SMA semi rigid RF cables with attenuation -2.5dB per meter at 20GHz.
- **Gaussmeter** = Hirst GM07 Handheld Tranverse Hall effect meter
- **Magnets** = 10x10x5mm Nickel-coated Neodymium magnets
- **MFLI** = Zurich Instruments MFLI Lock-in Amplifier
- **Cernox** = LakeShore CX-SD Cernox cryogenic temperature sensor
- Custom Coax breakout box to MIL spec connector for readout

8.2 B: Sample Fabrication Details

The substrate that was used came from 300nm SiO2 thermal oxide wafers. These were cut to roughly 8mm by 3mm pieces and cleaned in a cleanroom. This process involved drenching the substrate in acetone, leaving it inside an ultrasonic bath and rinsing it with isopropanol. The deposition was done using an e-beam evaporator. The non-capped samples were created in one cycle. The batch of capped samples were first created with a cobalt layer, on which the niobium and platinum was deposited for each sample individually. The average deposition parameters for the materials used are shown in Table 8.1.

Material	Chamber pressure (mbar)	Deposition rate (nm/s)	Chamber temperature
Cobalt	4.0E-08	0.1	RT
Niobium	2.5E-08	0.3	RT
Platinum	4.0E-08	0.1	RT

Figure 8.1: *Table showing the evaporation parameters per deposited material. Deposition rate and temperature were constant across different samples. Chamber pressure is approximate average per material.*

8.3 C: Measurement Parameters per Dataset

For all results shown in this report, the measurement parameters for the VNA are listed here. The parameters per dataset are shown in Figure 8.2. The common parameters across all measurements:

- Data type: S21 dB magnitude measurement
- Output power: -10dB
- Averaging factor: 4 sweeps continuous average

Dataset	Sweep start (GHz)	Sweep stop (GHz)	# points	Distance datapoints (MHz)	Bandwidth (kHz)	Average loss 4 to 6GHz (dB)
Co(30nm)Nb(30nm)Pt(5nm) at RT	0.001	7.25	5000	1.5	0.1	-9.1
Co(30nm)Nb(40nm) Cryo set 1	2	7	1000	5	1	-14
Co(30nm)Nb(20nm) Cryo Set 1	2.5	9.5	2000	3.5	1	-15.2
Co(30nm)Nb(xxnm) Additional set	3	8	2500	2	1	-12.7

Figure 8.2: *Table showing the VNA parameters per dataset as presented in this thesis.*

Bibliography

[1] J.-m. L. Beaujour, W. Chen, Andrew D. Kent, and J. Z. Sun. Ferromagnetic resonance study of polycrystalline cobalt ultrathin films. *Journal of Applied Physics*, 99(8), 4 2006.

[2] C. H. Bell, Sergey Milikisyants, Martina Huber, and J. Aarts. Spin Dynamics in a Superconductor-Ferromagnet Proximity System. *Physical Review Letters*, 100(4), 2 2008.

[3] A. K. Chan, M. Cubukcu, X. Montiel, Sachio Komori, Alex Vanstone, Juliet Thompson, G. K. Perkins, C. J. Kinane, Andrew J. Caruana, D. Boldrin, M. G. Blamire, Jason W. A. Robinson, Matthias Eschrig, Hidekazu Kurebayashi, and L. F. Cohen. Controlling spin pumping into superconducting Nb by proximity-induced spin-triplet Cooper pairs. *Communications Physics*, 6(1), 10 2023.

[4] Yi Chun Chen, D. S. Hung, Y. D. Yao, S. F. Lee, Huan Pei Ji, and Cheng Chia Yu. Ferromagnetic resonance study of thickness-dependent magnetization precession in Ni80Fe20 films. *Journal of Applied Physics*, 101(9), 5 2007.

[5] J. M. D. Coey. *Magnetism and Magnetic Materials*. cambridge University Press, 1 2010.

[6] F.D. Czeschka. Spin Currents in Metallic Nanostructures. Ph.D. thesis, 2011.

[7] Jimmy de Haan. Towards spin triplet superconducting junctions in a dynamic regime, 2019.

[8] Matthias Eschrig. Spin-polarized supercurrents for spintronics: a review of current progress. *Reports on Progress in Physics*, 78(10):104501, September 2015.

[9] Z. Frait. Ferromagnetic resonance in thin cobalt films. *Czechoslovak Journal of Physics/Czechoslovak journal of physics*, 11(5):360–368, 5 1961.

[10] Kun-Rok Jeon, Chiara Ciccarelli, A. J. Ferguson, Hidekazu Kurebayashi, L. F. Cohen, X. Montiel, Matthias Eschrig, Jason W. A. Robinson, and M. G. Blamire. Enhanced spin pumping into superconductors provides evidence for superconducting pure spin currents. *Nature Materials*, 17(6):499–503, 4 2018.

[11] Kun-Rok Jeon, Chiara Ciccarelli, Hidekazu Kurebayashi, L. F. Cohen, X. Montiel, Matthias Eschrig, Sachio Komori, Jason W. A. Robinson, and M. G. Blamire. Exchange-field enhancement of superconducting spin pumping. *Physical review*, 99(2), 1 2019.

[12] Sangita S. Kalarickal, Pavol KrivosÃk, Mingzhong Wu, Carl E. Patton, Michael L. Schneider, Pavel Kabos, Thomas J. Silva, and J. P. Nibarger. Ferromagnetic resonance linewidth in metallic thin films: Comparison of measurement methods. *Journal of Applied Physics*, 99(9), 5 2006.

[13] Kaveh Lahabi. Spin-triplet supercurrents of odd and even parity in nanostructured devices, 12 2018.

[14] Philip Louis. Broadband-Spectroscopy of magnetic materials at low temperatures, 2016.

[15] Ivan S. Maksymov and Mikhail Kostylev. Broadband stripline ferromagnetic resonance spectroscopy of ferromagnetic films, multilayers and nanostructures. *Physica E: Low-dimensional Systems and Nanostructures*, 69:253–293, 5 2015.

[16] Eric Montoya, Tommy McKinnon, Atieh Zamani, Erol Girt, and B. Heinrich. Broadband ferromagnetic resonance system and methods for ultrathin magnetic films. *Journal of Magnetism and Magnetic Materials*, 356:12–20, 4 2014.

[17] O. Mosendz, B. Kardasz, David S. Schmool, and B. Heinrich. Spin dynamics at low microwave frequencies in crystalline Fe ultrathin film double layers using co-planar transmission lines. *Journal of Magnetism and Magnetic Materials*, 300(1):174–178, 5 2006.

[18] RS. *Guidance on Selecting and Handling Coaxial RF Connectors used with Rohde and Schwarz Test Equipment*. Rohde and Schwarz GmbH and Co, 2015.

[19] RS. *RandS ZNL/ZNLE Vector Network Analyzers User Manual*. Rohde and Schwarz GmbH and Co, 20 edition, 2023.

[20] M. Trezza, S. L. Prischepa, C. Cirillo, R. Fittipaldi, M. Sarno, D. Sannino, P. Ciambelli, M. B. S. Hesselberth, S. K. Lazarouk, A. V. Dolbik, V. E. Borisenko, and C. Attanasio. Superconducting properties of Nb thin films deposited on porous silicon templates. *Journal of applied physics*, 104(8), 10 2008.

[21] Dyon van Dinter. Superconducting spintronics in the static and dynamic regime, 2021.

[22] Timotheus Verhagen. Magnetism and magnetization dynamics in thin film ferromagnets, 2014.

[23] V. V. Zagorodnii, Andrew Hutchison, Stephanie B. Hansen, Jue Chen, H.H. Gatzen, and Z. Celinski. Broad-band ferromagnetic resonance characterization of lossy ferromagnetic metallic elements. *Journal of Applied Physics*, 107(11), 6 2010.